THE UNIVERSITY of EDINBURGH

Edinburgh Research Explorer

Dual-modal Image Reconstruction for Electrical Impedance Tomography with Overlapping Group Lasso and Laplacian Regularization

Citation for published version:
Liu, Z, Gu, H, Chen, Z, Bagnaninchi, PO & Yang, Y 2023, 'Dual-modal Image Reconstruction for Electrical Impedance Tomography with Overlapping Group Lasso and Laplacian Regularization', *IEEE Transactions on Biomedical Engineering*, pp. 1-12. https://doi.org/10.1109/TBME.2023.3243781

Digital Object Identifier (DOI):
10.1109/TBME.2023.3243781

Link:
Link to publication record in Edinburgh Research Explorer

Document Version:
Peer reviewed version

Published In:
IEEE Transactions on Biomedical Engineering

General rights
Copyright for the publications made accessible via the Edinburgh Research Explorer is retained by the author(s) and / or other copyright owners and it is a condition of accessing these publications that users recognise and abide by the legal requirements associated with these rights.

Take down policy
The University of Edinburgh has made every reasonable effort to ensure that Edinburgh Research Explorer content complies with UK legislation. If you believe that the public display of this file breaches copyright please contact openaccess@ed.ac.uk providing details, and we will remove access to the work immediately and investigate your claim.

OPEN ACCESS

Download date: 10. Mar. 2023

Dual-modal Image Reconstruction for Electrical Impedance Tomography with Overlapping Group Lasso and Laplacian Regularization

Zhe Liu, *Graduate Student Member, IEEE*, Hengjia Gu, Zhou Chen, *Student Member, IEEE*, Pierre Bagnaninchi, Yunjie Yang, *Member, IEEE*

***Abstract*— Objective: Electrical Impedance Tomography (EIT) is a promising biomedical imaging modality, yet EIT image reconstruction remains an open challenge due to its severe ill-posedness. High-quality EIT image reconstruction algorithms are desired. Methods: This paper reports a segmentation-free dual-modal EIT image reconstruction algorithm that uses Overlapping Group Lasso and Laplacian (OGLL) regularization. An overlapping group lasso penalty is constructed based on conductivity change properties and encodes the imaging targets' structural information obtained from an auxiliary imaging modality that provides structural images of the sensing region. We introduce Laplacian regularization to alleviate the artifacts caused by group overlapping. Results: The performance of OGLL is evaluated and compared with single-modal and dual-modal image reconstruction algorithms using simulation and real-world data. Quantitative metrics and visualized images confirm the superiority of the proposed method in terms of structure preservation, background artifact (BA) suppression, and conductivity contrast differentiation. Conclusion: This work proves the effectiveness of OGLL in improving EIT image quality. Significance: This study demonstrates that EIT has the potential to be adopted in quantitative tissue analysis by using such dual-modal imaging approaches.**

***Index Terms*— Dual-modal imaging, Electrical Impedance Tomography, image reconstruction, overlapping group lasso, Laplacian regularization**

I. Introduction

BIOMEDICAL imaging aims to visualize internal structures or functions of the human body, tissues or cells. Different imaging modalities estimate different parameters and/or properties, thus, revealing different aspects of organism status. Among existing biomedical imaging modalities such as Electrical Impedance Tomography (EIT) , Positron Emission Tomography (PET) [3], and Optical Coherence Tomography (OCT) [4], EIT has demonstrated its unique advantages in non-destructive, non-radioactive imaging, making it suitable for in vivo imaging [1]–[3]. After stimulating with small electric fields and recording the voltage between electrodes, EIT reconstructs the conductivity distribution of the region of interest. EIT images can serve as evidence for clinical or medical analysis and diagnosis, as different tissues or distinct physiological states are characterised by different conductivity. For instance, EIT has been applied to lung function monitoring [6] [7], nerve imaging [8] [9] and 3D cell culture monitoring [10]–[12]. However, EIT suffers from low image qualities concerning structure preservation, background artefact (BA) suppression, and differentiation of conductivity contrasts, preventing it from quantitative analyses, thus limiting its further applications in biomedical fields.

Various measures could improve EIT image quality, such as advancing instrumentation [13] [14], optimizing sensor design and refining sensing strategy [15]. Also central to EIT performance are the image reconstruction algorithms aiming to solve the inverse problem, including Total Variation (TV) regularization [16]–[18], sparse regularization [19]–[21], multiplicative regularization [22], group sparsity regularization [23] [24], the D-bar method [25] [26], Sparse Bayesian Learning [27] [28], GREIT [29] and learning-based methods [30]–[32]. These algorithms have achieved remarkable success in improving EIT image quality. However, these methods are mainly single-modal-based and only leverage EIT data.

Another class of approaches is dual-modal or multi-modal-based. These approaches combine EIT with one or multiple complementary imaging modalities (referred to as auxiliary modalities). For example, it was shown that EIT-ultrasound imaging has the benefit of improving EIT image quality [33]–[35]. Li et al. encoded structural information from the CT image using Cross-Gradient regularization and employed the constructed regularization term to confine EIT inversion [36]. Both Gong et al. [37], and Liu et al. [38] proposed to incorporate the prior information of the auxiliary image into EIT inversion through a non-overlapping group lasso. The difference is that Gong et al. group conductivity changes based on K-Means clustering of auxiliary image pixels, while Liu et al. generate groups based on the semantic segmentation of the auxiliary image. Liu et al. further developed a segmentation-free dual-modal algorithm using Kernel Method [39] and reported the first exploration of learning-based methods for dual-modal EIT imaging [40].

Compared to single-modal approaches, previous studies

Z. Liu, H. Gu, Z. Chen and Y. Yang are with the Institute for Digital Communications, School of Engineering, The University of Edinburgh, Edinburgh, UK, EH9 3JL (Corresponding author: Yunjie Yang, e-mail: y.yang@ed.ac.uk).

P. Bagnaninchi is with the Centre for Regenerative Medicine, Institute for Regeneration and Repair, The University of Edinburgh, Edinburgh, UK, EH16 4UU.

demonstrate that multi-modal imaging could further improve image quality. Here, we propose an image reconstruction algorithm based on overlapping group lasso and Laplacian regularization (named OGLL). OGLL is not confined to a specific auxiliary imaging modality. On the contrary, we discuss the approach in general, as OGLL can be applied to various dual-modal imaging setups where the auxiliary imaging modality provides structural information, such as CT scanning for lung measurements or optical imaging for cell clusters. Similar to [37] and [38], OGLL introduces the structural information of the auxiliary image into EIT inversion through group lasso. Differently, OGLL firstly adopts the overlapping strategy and groups conductivity changes based on local characteristics of the auxiliary image. Thus, it eliminates the need to semantically segment the imaging targets in [38]. In addition, since the image quality is significantly affected by the non-overlapping partition of conductivity changes, previous methods such as [37] are unstable due to the uncertainty of grouping results. OGLL tackles such issues by generating parameter-controlled deterministic groups. In summary, the advantages of OGLL are as follows:

- We first incorporate the overlapping group lasso into dual-modal EIT image reconstruction. OGLL demonstrates considerable improvements in structure preservation, background artifact suppression, and differentiation of conductivity contrasts compared with other single-modal and multi-modal image reconstruction algorithms.
- OGLL introduces a new grouping method, which is regular and controllable, leading to stable grouping results. As OGLL allows group overlapping, the requirement of fine-designed grouping rules and certain prior information (e.g., the number of groups) for non-overlapping grouping is unnecessary.
- The Laplacian regularization in OGLL can alleviate the artifacts caused by group overlapping (abbreviated as GOA). It enables flexible grouping strategies for OGLL, i.e., using the search window with various sizes and step lengths.

II. Principle of EIT

Consider an imaging region $\mho \subset \mathbb{R}^D$, $D = 2$ or 3, E electrodes represented by $\{e_i\}_{i=1}^E$ are evenly attached on its boundary $\partial\mho$. EIT consists of two subproblems - forward and inverse problems.

A. Forward Problem

Given a known conductivity distribution, the forward problem of EIT calculates the electrical potential distribution within the sensing region. Assuming $\sigma(p) \in \mathbb{R}$, $p \in \mho$, denotes the continuous-space real-valued conductivity, the commonly-used Complete Electrode Model (CEM) [41] is formulated as:

$$\nabla \cdot [\sigma(p)\nabla u(p))] = 0,\ p \in \mho \tag{1}$$

$$u(p) + z_i\sigma(p)\frac{\partial u(p)}{\partial \widehat{n}} = U_i,\ p \in e_i,\ i = 1,\ 2,\ ...,\ E \tag{2}$$

$$\int_{e_i} \sigma(p)\frac{\partial u(p)}{\partial \widehat{n}} d\ell = I_i,\ i = 1,\ 2,\ ...,\ E \tag{3}$$

$$\sigma(p)\frac{\partial u(p)}{\partial \widehat{n}} = 0,\ p \in \partial\mho \backslash \bigcup_{i=1}^{E} e_i \tag{4}$$

$$\sum_{i=1}^{E} I_i = 0,\ \sum_{i=1}^{E} U_i = 0, \tag{5}$$

where $u(p)$ denotes the electrical potential in the sensing region and $\widehat{n}$ represents the outer unit normal of $\partial\mho$. z_i, U_i and I_i are the contact impedance, electrical potential, and the injected current on e_i, respectively. Equation (5) guarantees the existence and uniqueness of the solution of (1).

B. Inverse Problem

We adopt the time-difference imaging approach, and describe the inverse problem in this specific setup. The mesh adopted for circular sensing region is illustrated in Fig. 1 (a). The linearized EIT forward model considered in this study is described by

$$\mathbf{V} = \mathbf{J}\boldsymbol{\sigma}, \tag{6}$$

where $\mathbf{V} = -\frac{\mathbf{V}_o - \mathbf{V}_r}{\mathbf{V}_r}$ and $\boldsymbol{\sigma} = \frac{\boldsymbol{\sigma}_o - \boldsymbol{\sigma}_r}{\boldsymbol{\sigma}_r}$. $\mathbf{V}_o \in \mathbb{R}^M$ and $\mathbf{V}_r \in \mathbb{R}^M$ represent the measured voltages at the observation and reference time points. $\boldsymbol{\sigma}_o \in \mathbb{R}^N$ and $\boldsymbol{\sigma}_r \in \mathbb{R}^N$ account for the conductivity distribution at the observation and reference time points, respectively. At the reference time point, the conductivity distribution is homogeneous. N is the number of pixels of the EIT image and M is the number of measurements. Throughout the paper, vector division means element-wise division. $\mathbf{J} \in \mathbb{R}^{M\times N}$ denotes the normalised sensitivity matrix. Refer to Appendix for the derivation of (6).

The general approach to formulate the inverse problem of EIT, which estimates $\boldsymbol{\sigma}$ subject to the (6), is expressed by:

$$\begin{aligned} \min_{\boldsymbol{\sigma}} \quad & R(\boldsymbol{\sigma}) \\ \text{s.t.} \quad & \mathbf{J}\boldsymbol{\sigma} = \mathbf{V}, \end{aligned} \tag{7}$$

where $R:\ \mathbb{R}^n \to \mathbb{R}$ denotes the regularization function, which encodes the prior information.

III. Methods

OGLL comprises two steps, i.e., conductivity grouping and image reconstruction. Conductivity grouping is the key to constructing the group lasso regularization term. The idea of using group lasso encoding the prior information is based on the observation that, in biomedical applications, the EIT image usually shows local similarity for biological tissues with similar function or anatomy. Specifically, in time-difference imaging, the zero changes of the conductivity and non-zero akin changes of the conductivity typically present the property of local clustering. In addition, the group lasso can promote sparsity on the group level and discourage sparsity within

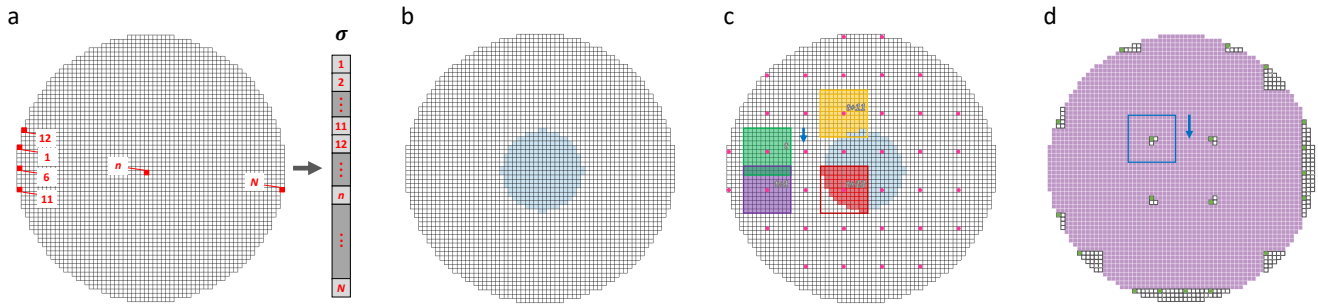

Fig. 1. Illustration of EIT inverse mesh and overlapping groups. (a) is the mesh for EIT inverse problem which consists of 3228 simplexes. (b) ∼ (d) show a grouping example. (b) is an example with one inclusion which is indicated by blue simplexes in (b) and (c). In (c), the colored square boundary defines the search window and the colored region means grouped pixels. Different colors represent different groups. Fuchsia circular disks denote all centers of search windows in the first grouping stage. In (d), light purple region shows grouped pixels (may belong to different groups) in the first grouping stage. The remaining pixels are ungrouped. Green circular disks stand for centers of search windows and blue square boundary represents the search window in the second grouping stage. Blue arrows in (c) and (d) indicate the moving direction of the search window.

each group [44]. Therefore, grouping similar conductivity changes can mitigate the ill-posedness of the EIT inversion and improve reversibility. For the image reconstruction step, OGLL solves the optimization problem using the Alternating Direction Method of Multipliers (ADMM) [45]. More details of OGLL are as follows.

A. Conductivity Grouping

In OGLL, conductivity grouping is based on the pixel similarity over the auxiliary image. To avoid ambiguity, we strictly impose the size of the auxiliary image is the same as that of the EIT image. A pixel at the same position in both the EIT and auxiliary images corresponds to the same point of the imaging target. Usually, images generated by the auxiliary modality like CT are larger than EIT images, and the auxiliary images are acquired by down-sampling them into the EIT image size.

Before grouping, we predefine a set of feature vectors $\{\mathbf{f}_n \in \mathbb{R}^W,\ W \geq 1\}_{n=1}^N$ to characterize the pixels of the EIT image and a measure function $\iota : \mathbb{R}^W \times \mathbb{R}^W \to \mathbb{R}$ to evaluate the similarity between different pixels of the EIT image. In general, $\mathbf{f}_n$ and ι are selected based on the characteristics of the auxiliary image. For example, intensity values of the 3×3 window centered at the nth pixel of the auxiliary image can form the 9-element feature vector for the nth pixel of the EIT image. In this study, $\mathbf{f}_n$ is defined as the nth pixel intensity of the auxiliary image, and the below exponential function is selected as the similarity measure:

$$\iota(\mathbf{f}_n, \mathbf{f}_k) = \exp(-||\mathbf{f}_n - \mathbf{f}_k||^2), \tag{8}$$

where $||\cdot||$ denotes the l_2 norm. We define that two elements of $\boldsymbol{\sigma}$ belong to the same group if ι of their feature vectors is larger than a pre-defined positive threshold φ.

The grouping process is composed of two stages. In the first stage, a $s \times s$ window (named the search window) slides over the auxiliary image. The sliding direction is from top to bottom then from left to right. s is a positive odd number. The horizontal and vertical step sizes (denoted by q) are the same and should be pre-specified. At each position, in the search window, elements of $\boldsymbol{\sigma}$ whose ι with respect to the center pixel larger than φ are categorized into the same group. To guarantee as many elements of $\boldsymbol{\sigma}$ to be grouped as possible in the first stage, $1 \leq q \leq s$ is required.

After the first grouping stage, some elements of $\boldsymbol{\sigma}$ may not be grouped. Therefore, in the second stage, we first locate the ungrouped element of the $\boldsymbol{\sigma}$ which has the lowest row and column indexes in the EIT image, and group the elements of $\boldsymbol{\sigma}$ in the $s \times s$ search window centered at the located element with the same φ used in the first stage. Then, for the remaining ungrouped elements of $\boldsymbol{\sigma}$, we continue locating the ungrouped element which has the lowest row and column indexes and perform the same grouping approach. We repeat this operation until all elements of $\boldsymbol{\sigma}$ are grouped. In summary, the grouping process can be simply considered as sliding twice the $s \times s$ search window along the same direction over the auxiliary images to group all elements of $\boldsymbol{\sigma}$.

During the grouping process, overlapping is allowed, leading to the grouping result of:

$$\{\boldsymbol{\sigma}_{g_1},\ \boldsymbol{\sigma}_{g_2},\ \ldots,\ \boldsymbol{\sigma}_{g_G}\}, \tag{9}$$

where G is the number of groups, $1 \leq G \leq N$; $\boldsymbol{\sigma}_{g_\varsigma} \bigcap \boldsymbol{\sigma}_{g_\tau} \neq \phi$ or $\boldsymbol{\sigma}_{g_\varsigma} \bigcap \boldsymbol{\sigma}_{g_\tau} = \phi$ if $\varsigma \neq \tau$, and $\bigcup_{\varepsilon=1}^{G} \boldsymbol{\sigma}_{g_\varepsilon} = \boldsymbol{\sigma}$. τ, ς and ε are group indicators. The grouping method is simple and regular, and the result is controllable by tuning s and q once $\mathbf{f}_n$ and ι are determined. An example of the grouping process is illustrated in Fig. 1 (b) ∼ (d). Finally, the overlapping group lasso regularization term can be expressed by the following $l_{2,1}$ norm:

$$l_{2,1} = \sum_{\varepsilon=1}^{G} \psi_\varepsilon ||\boldsymbol{\sigma}_{g_\varepsilon}||, \tag{10}$$

where, $\psi_\varepsilon > 0$ represents the weight for the εth group.

B. The Laplacian Regularization

We will show later that group overlapping may lead to artefacts (see Fig. 7), i.e. the GOA, especially for relatively small s and q. The GOA increases the rapid pixel intensity changes in the reconstructed EIT image. Inspired by [46], the Laplacian regularization term is included to alleviate the negative influence of GOA. The continuous Laplacian of an

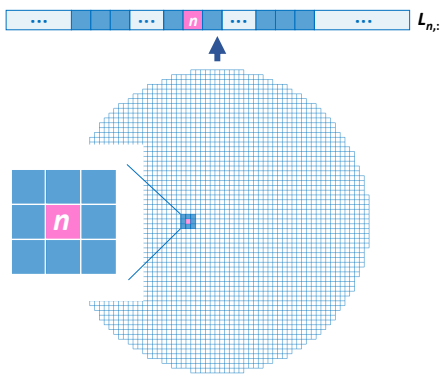

Fig. 2. Principle of constructing the Laplacian matrix: $\boldsymbol{L}_{\boldsymbol{n},:}$ denotes the $\boldsymbol{n}^{\text{th}}$ row of $\boldsymbol{L}$. The pink square represents the kernel center, which is also located at the $\boldsymbol{n}^{\text{th}}$ pixel of the EIT image. Dark blue squares denote the 8-neighbors of the $\boldsymbol{n}^{\text{th}}$ pixel. In $\boldsymbol{L}_{\boldsymbol{n},:}$, the value at the pink pixel is set to 8 and that at the dark blue pixel is set to -1. Other values at light blue pixels are filled by zeros.

Algorithm 1 Dual-modal EIT Image Reconstruction based on OGLL

Input: Auxiliary image, $\mathbf{J}$, $\mathbf{V}$, s, q, φ, θ, α, β_1,β_2, η_1, η_2, $t_{\max}$, ϑ.

Output: Calculated conductivity distribution.

Initialize: $\boldsymbol{\sigma} \leftarrow \mathbf{0}_N$, $\mathbf{z} \leftarrow \mathbf{0}_\Xi$, $\boldsymbol{\lambda}_1 \leftarrow \mathbf{0}_\Xi$, $\boldsymbol{\lambda}_2 \leftarrow \mathbf{0}_M$.

1: Conductivity grouping to construct (10) according to A, Section III.
2: **while** stopping criteria unsatisfied **do**
3: Solve problem (15) by (16);
4: Solve problem (17) by (19);
5: Update $\boldsymbol{\lambda}_1$ by (21);
6: Update $\boldsymbol{\lambda}_2$ by (22).
7: **end while**

image $\mathcal{I}(x, y)$ is defined as:

$$\mathcal{L}(x, y) = \frac{\partial^2 \mathcal{I}(x, y)}{\partial x^2} + \frac{\partial^2 \mathcal{I}(x, y)}{\partial y^2}, \tag{11}$$

where $x \in \mathbb{R}$ and $y \in \mathbb{R}$ are coordinates of the image. As the Laplacian is sensitive to rapid image intensity changes, we might penalize the Laplacian of the EIT image to reduce GOA. For digital images, a small discrete convolutional kernel is usually adopted to approximate (11) and the discrete Laplacian can be calculated by the convolution. In this work, a 3×3 kernel is chosen and the vectorized discrete Laplacian of the EIT image can be formulated as $\mathbf{L}\boldsymbol{\sigma}$, where $\mathbf{L} \in \mathbb{R}^{N \times N}$ is the Laplacian matrix. The detailed description of the kernel and the Laplacian matrix construction is illustrated in Fig. 2.

C. Image Reconstruction Based on OGLL

OGLL can be formulated as the following optimization problem:

$$\begin{aligned} \min_{\boldsymbol{\sigma}} \quad & \sum_{\varepsilon=1}^{G} \psi_\varepsilon ||\boldsymbol{\sigma}_{g_\varepsilon}|| + \frac{\theta}{2}||\mathbf{L}\boldsymbol{\sigma}||^2 \\ \text{s.t.} \quad & \mathbf{J}\boldsymbol{\sigma} = \mathbf{V}, \end{aligned} \tag{12}$$

where $\theta > 0$ denotes the parameter for the Laplacian regularization. (12) can be effectively solved by ADMM. By introducing an auxiliary variable $\mathbf{z} \in \mathbb{R}^\Xi$, (12) is reformulated as:

$$\begin{aligned} \min_{\boldsymbol{\sigma}, \mathbf{z}} \quad & \sum_{\varepsilon=1}^{G} \psi_\varepsilon ||\mathbf{z}_{g_\varepsilon}|| + \frac{\theta}{2}||\mathbf{L}\boldsymbol{\sigma}||^2 \\ \text{s.t.} \quad & \mathbf{z} = \mathbf{F}\boldsymbol{\sigma}, \ \mathbf{J}\boldsymbol{\sigma} = \mathbf{V}, \end{aligned} \tag{13}$$

where $\mathbf{F} \in \mathbb{R}^{\Xi \times N}$, $N \leq \Xi \leq N^2$, is a (0, 1) matrix and each row has an unique 1. If n^{th} element of $\boldsymbol{\sigma}$ belongs to $\mathcal{G}$ groups, $1 \leq \mathcal{G} \leq G$, there are $\mathcal{G}$ rows of $\mathbf{F}$ in each of which the nth element is 1. Thus, the transformation of $\mathbf{F}$ duplicates the nth element of $\boldsymbol{\sigma}$ $\mathcal{G}$ times and integrates them into $\mathbf{z}$. In other words, although elements of $\boldsymbol{\sigma}$ are overlapped, elements of $\mathbf{z}$ are completely non-overlapped. Furthermore, $\mathbf{F}^T\mathbf{F}$ is a diagonal matrix, whose n^{th} diagonal element represents the number of groups the nth element of $\boldsymbol{\sigma}$ belongs to. Especially in the case of non-overlapping grouping, $\mathbf{F}$ becomes a $N \times N$ identity matrix. To solve (13), the augmented Lagrangian equation is firstly constructed:

$$\begin{aligned} \min_{\boldsymbol{\sigma}, \mathbf{z}, \boldsymbol{\lambda}_1, \boldsymbol{\lambda}_2} \quad & \sum_{\varepsilon=1}^{G} \psi_\varepsilon ||\mathbf{z}_{g_\varepsilon}|| + \frac{\theta}{2}||\mathbf{L}\boldsymbol{\sigma}||^2 \\ & - \boldsymbol{\lambda}_1^T(\mathbf{z} - \mathbf{F}\boldsymbol{\sigma}) + \frac{\beta_1}{2}||\mathbf{z} - \mathbf{F}\boldsymbol{\sigma}||^2 \\ & - \boldsymbol{\lambda}_2^T(\mathbf{J}\boldsymbol{\sigma} - \mathbf{V}) + \frac{\beta_2}{2}||\mathbf{J}\boldsymbol{\sigma} - \mathbf{V}||^2, \end{aligned} \tag{14}$$

where $\boldsymbol{\lambda}_1 \in \mathbb{R}^\Xi$, and $\boldsymbol{\lambda}_2 \in \mathbb{R}^M$ are Lagrange multipliers and $\beta_1 > 0$ and $\beta_2 > 0$ are penalty parameters. Then, (14) can be split into the $\boldsymbol{\sigma}$-subproblem and the $\mathbf{z}$-subproblem, which are solved separately. From (14), the $\boldsymbol{\sigma}$-subproblem can be expressed as:

$$\begin{aligned} \boldsymbol{\sigma}^t = \ & \arg\min_{\boldsymbol{\sigma}} \ \frac{\theta}{2}||\mathbf{L}\boldsymbol{\sigma}||^2 + (\boldsymbol{\lambda}_1^{t-1})^T\mathbf{F}\boldsymbol{\sigma} \\ & + \frac{\beta_1}{2}||\mathbf{z}^{t-1} - \mathbf{F}\boldsymbol{\sigma}||^2 - \boldsymbol{\lambda}_2^T\mathbf{J}\boldsymbol{\sigma} + \frac{\beta_2}{2}||\mathbf{J}\boldsymbol{\sigma} - \mathbf{V}||^2, \end{aligned} \tag{15}$$

where superscript $t = 1, 2, 3, \ldots$ represents the iteration number. In this work, (15) is solved by one-step gradient descent and its iteration equation is expressed as:

$$\begin{aligned} \boldsymbol{\sigma}^t = \ & \boldsymbol{\sigma}^{t-1} - \alpha \left[(\theta\mathbf{L}^T\mathbf{L} + \beta_1\mathbf{F}^T\mathbf{F} + \beta_2\mathbf{J}^T\mathbf{J})\boldsymbol{\sigma}^{t-1} \right. \\ & \left. - (\beta_1\mathbf{F}^T\mathbf{z}^{t-1} - \mathbf{F}^T\boldsymbol{\lambda}_1^{t-1} + \beta_2\mathbf{J}^T\mathbf{V} + \mathbf{J}^T\boldsymbol{\lambda}_2^{t-1}) \right], \end{aligned} \tag{16}$$

where α is the iteration step length.

The $\mathbf{z}$-subproblem can also be deduced from (14) and it is formulated as:

$$\mathbf{z}^t = \arg\min_{\mathbf{z}} \sum_{\varepsilon=1}^{G} \psi_\varepsilon ||\mathbf{z}_{g_\varepsilon}|| - (\boldsymbol{\lambda}_1^{t-1})^T\mathbf{z} + \frac{\beta_1}{2}||\mathbf{z} - \mathbf{F}\boldsymbol{\sigma}^t||^2. \tag{17}$$

Equation (17) is equivalent to solving the below problem:

$$\begin{aligned} \mathbf{z}^t = \ & \arg\min_{\mathbf{z}} \sum_{\varepsilon=1}^{G} [\psi_\varepsilon ||\mathbf{z}_{g_\varepsilon}|| \\ & + \frac{\beta_1}{2}||\mathbf{z}_{g_\varepsilon} - (\mathbf{F}\boldsymbol{\sigma}^t)_{g_\varepsilon} - \frac{1}{\beta_1}(\boldsymbol{\lambda}_1^{t-1})_{g_\varepsilon}||^2], \end{aligned} \tag{18}$$

TABLE I
PARAMETER SETTINGS OF OGLL AND KMGS FOR BLOCKY PHANTOM IMAGING

		η_1	η_2	$t_{\max}$	ϑ	φ	s	q	θ	α	β_1	β_2
KMGS	Case 1	1.2944	1.2944	1000	10^{-7}	\	\	\	0	0.01	3	3
	Case 2	1.2944	1.2944	1000	10^{-7}	\	\	\	0	0.02	3	3
	Case 3	1.2944	1.2944	1000	10^{-7}	\	\	\	0	0.02	0.2	0.2
OGLL-NGOA	Case 1	1.2944	1.2944	1000	10^{-7}	0.95	29	8	0	0.006	0.5	0.5
	Case 2	1.2944	1.2944	1000	10^{-7}	0.95	81	8	0	0.0007	0.1	0.1
	Case 3	1.2944	1.2944	1000	10^{-7}	0.95	21	4	0	0.002	0.8	0.8
OGLL-GOA	Case 1	1.2944	1.2944	1000	10^{-7}	0.95	9	3	0.35	0.01	3.5	3.5
	Case 2	1.2944	1.2944	1000	10^{-7}	0.95	11	3	0.3	0.03	1	1
	Case 3	1.2944	1.2944	1000	10^{-7}	0.95	5	1	0.2	0.008	5	5

which can be solved using group-wise soft thresholding:

$$(\mathbf{z}^t)_{g_\varepsilon} = \max(0,\ ||\boldsymbol{\ell}_\varepsilon|| - \frac{\psi_\varepsilon}{\beta_1})\frac{\boldsymbol{\ell}_\varepsilon}{||\boldsymbol{\ell}_\varepsilon||},\ \varepsilon = 1,\ 2,\ ...,\ G, \tag{19}$$

where $\boldsymbol{\ell}_\varepsilon$ is given by:

$$\boldsymbol{\ell}_\varepsilon = (\mathbf{F}\boldsymbol{\sigma}^t)_{g_\varepsilon} + \frac{1}{\beta_1}(\boldsymbol{\lambda}_1^{t-1})_{g_\varepsilon},\ \varepsilon = 1,\ 2,\ ...,\ G. \tag{20}$$

Afterwards, the Lagrange multipliers are updated:

$$\boldsymbol{\lambda}_1^t = \boldsymbol{\lambda}_1^{t-1} - \eta_1\beta_1(\mathbf{z}^t - \mathbf{F}\boldsymbol{\sigma}^t), \tag{21}$$

$$\boldsymbol{\lambda}_2^t = \boldsymbol{\lambda}_2^{t-1} - \eta_2\beta_2(\mathbf{J}\boldsymbol{\sigma}^t - \mathbf{V}), \tag{22}$$

where $\eta_1 > 0$ and $\eta_2 > 0$ are iteration step lengths. The stopping criteria are defined by two conditions. The first one is the maximum iteration $t_{\max} \in \mathbb{Z}^+$ and the second one is the tolerance $\vartheta > 0$ which is defined as:

$$\frac{||\boldsymbol{\sigma}^{t+1} - \boldsymbol{\sigma}^t||}{||\boldsymbol{\sigma}^t||} < \vartheta. \tag{23}$$

If any of the conditions is satisfied, OGLL will stop. We initialize $\boldsymbol{\sigma}$, $\mathbf{z}$, $\boldsymbol{\lambda}_1$ and $\boldsymbol{\lambda}_2$ with zero vectors. The implementation of OGLL is summarised in **Algorithm 1**.

Remarks: $\mathbf{0}_{\cdot}$ represents the column 0-vector and the subscript accounts for its size. In this paper, the weights ψ_ε is always set as 1.

IV. SIMULATION STUDY

In this section, we conduct numerical simulation to analyse the performance of the OGLL method. First, based on blocky phantoms, we compare OGLL with standard Tikhonov regularization [47], Structure-Aware Sparse Bayesian Learning (SA-SBL) [27], Kernel Method [39], and the dual-modal algorithm in [37] (named KMGS in this paper), and discuss the properties of the OGLL. Moreover, the performance of the given algorithms are compared based on thorax imaging. For a fair comparison, ADMM optimization for KMGS is implemented the same as in OGLL while the grouping method remains identical to that in the original paper.

A. Quantitative Metrics

Image Relative Error (Err) and Mean Structural Similarity Index (MSSIM) [48] are selected as image quality indicators. Err measures the accuracy of conductivity estimation of an algorithm, which is defined as:

$$\text{Err} = \frac{||\boldsymbol{\sigma}_{\text{est}} - \boldsymbol{\sigma}_{\text{true}}||}{||\boldsymbol{\sigma}_{\text{true}}||}, \tag{24}$$

where $\boldsymbol{\sigma}_{\text{est}}$ and $\boldsymbol{\sigma}_{\text{true}}$ are estimated and ground truth conductivity vectors, respectively. MSSIM measures the structure preservation, which is defined by:

$$\text{MSSIM} = \frac{1}{N}\sum_n \frac{(2\boldsymbol{\mu}_{\text{est}}\boldsymbol{\mu}_{\text{true}} + \Gamma_1)\,(2\boldsymbol{\delta}_{\text{est,true}} + \Gamma_2)}{(\boldsymbol{\mu}_{\text{est}}^2 + \boldsymbol{\mu}_{\text{true}}^2 + \Gamma_1)\,(\boldsymbol{\delta}_{\text{est}}^2 + \boldsymbol{\delta}_{\text{true}}^2 + \Gamma_2)}, \tag{25}$$

where $\boldsymbol{\mu}_{\text{est}} = \boldsymbol{\mu}_{\text{est}}(n)$ and $\boldsymbol{\mu}_{\text{true}} = \boldsymbol{\mu}_{\text{true}}(n)$ denote the local means of the nth pixel, and $\boldsymbol{\delta}_{\text{est}} = \boldsymbol{\delta}_{\text{est}}(n)$ and $\boldsymbol{\delta}_{\text{true}} = \boldsymbol{\delta}_{\text{true}}(n)$ stand for the standard deviation of the nth pixel for the estimated conductivity change image and the ground truth image sequentially. $\boldsymbol{\delta}_{\text{est,true}} = \boldsymbol{\delta}_{\text{est,true}}(n)$ accounts for the cross covariance between the estimated conductivity change image and the ground truth image at the nth pixel. $\Gamma_1 = (U_1B)^2$ and $\Gamma_2 = (U_2B)^2$ are constants, where U_1, U_2 and B are set as 0.01, 0.03 and 1 respectively. More details of MSSIM can refer to [48].

B. Blocky Phantom Imaging

1) Modelling: We modelled the 16-electrode EIT sensor and added various inclusions as imaging targets. The resulting three types of conductivity distributions are labelled as case 1, case 2 and case 3. The simulated true conductivity images are illustrated in the first column of Fig. 3 and they correspond to case 1 $\sim$ 3 sequentially from top to bottom. For all cases, the background conductivity is set to 2 S/m. There are two rectangular inclusions for case 1. The conductivity of the left rectangle is set to 3.2 S/m and that of the right rectangle is set to 1.4 S/m. Case 2 simulates a huge circular inclusion whose conductivity is set to 0.5 S/m. For case 3, the conductivity of the uppermost smallest circular inclusion is set to 1.4 S/m. Starting from the rightest inclusion, the conductivity of the rest four inclusions are clockwise set to 1.4 S/m, 0.4 S/m, 0.9 S/m and 0.9 S/m. The auxiliary images are also simulated by assigning digit 1 to pixels of the inclusions and the background pixels are set to 0.5. The generated auxiliary images are illustrated in the first row of Fig. 4.

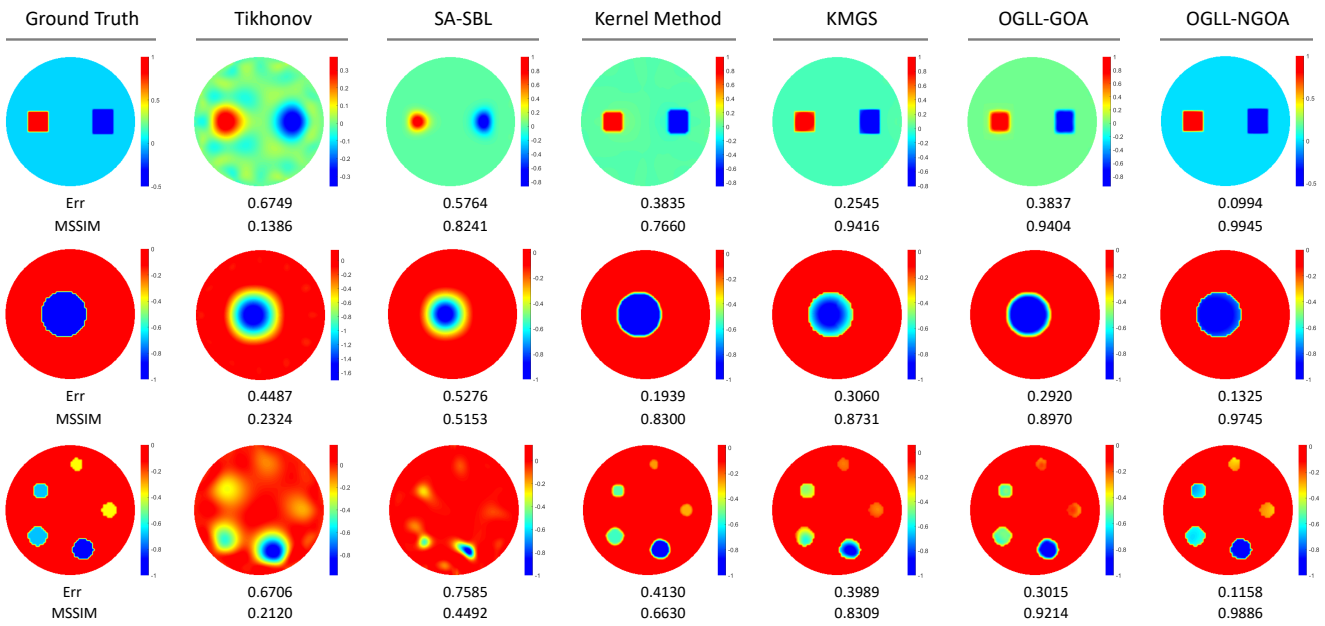

Fig. 3. Image reconstruction results based on blocky phantoms. Images from top to bottom correspond to case 1, case 2 and case 3, respectively. For case 1, the number of groups is 47 for OGLL-NGOA and is 76 for OGLL-GOA; for case 2, the number of groups is 47 for OGLL-NGOA and is 360 for OGLL-GOA; and for case 3, the number of groups is 201 for OGLL-NGOA and is 3228 for OGLL-GOA.

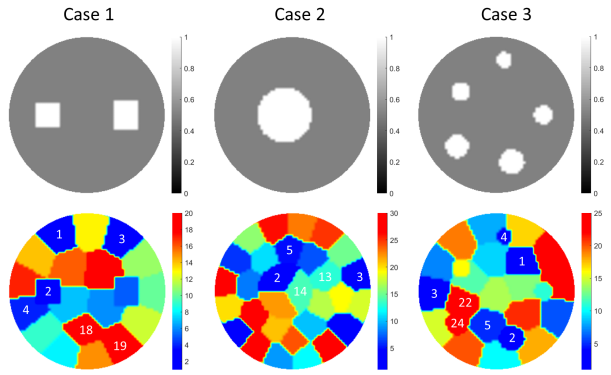

Fig. 4. Images in the first row are simulated auxiliary images and those in the second row are results of modified K-Means in KMGS. The number of clusters is 20, 30, and 25 for case 1, case 2 and case 3 respectively.

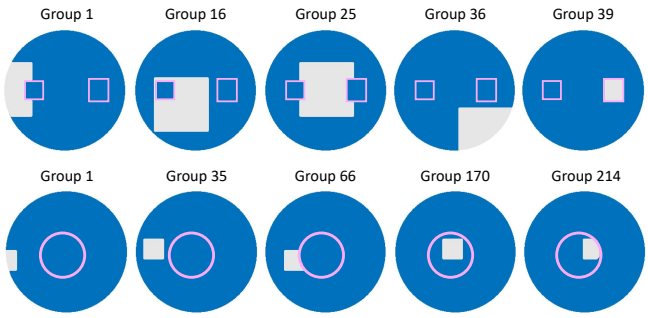

Fig. 5. Examples of grouping results of OGLL. The first row is part of the results based on the parameters of case 1 of OGLL-NGOA in Table I and there are 47 groups in total. The second row is part of the results based on the parameters of case 2 of OGLL-GOA in Table I and there are 360 groups in total. For each image, pixels in the white region belong to the same group. Pink curves represent the boundaries of inclusions.

2) Parameter Settings: Parameters for each algorithm are selected based on trials to obtain the results as best as possible. The regularization parameters of Tikhonov regularization are set as 0.00001, 0.0001, and 0.0003 for case 1, case 2, and case 3, respectively. For SA-SBL, the maximum iteration number, tolerance, and cluster size are set as 5, 10^{-5}, and 4 for all cases. The pattern coupling factors are set as 0.3, 2, and 0.8 for cases 1, 2, and 3 sequentially. For Kernel Method, all parameters are the same for the three cases. The feature window size and the search window size are set as 3 and 21, respectively. The number of nearest neighbors kNN is set as 441, and the variance of the Gaussian kernel is fixed as 20. In addition, the maximum iteration number is set as 500, and the iteration step for the gradient is selected as 10. For all cases, KMGS takes the same weighting parameter (0.01) for modified K-Means clustering, and the number of clusters is set to 20, 30, and 25 for cases 1, 2, and 3.

In later discussions, we group conductivities based on two types of search windows. One type of search windows usually causes the GOA phenomenon if we set θ to 0. The results based on this type of search windows are labeled as OGLL-GOA. The other type of search windows will not result in the GOA phenomenon if we set θ to 0, and the results are labeled as OGLL-NGOA. Usually, the search window size of OGLL-NGOA is larger than that of OGLL-GOA. When we mention OGLL, we refer to both OGLL-GOA and OGLL-NGOA. For a specific case, parameters for OGLL-GOA and OGLL-NGOA are usually different. Detail settings of OGLL-GOA and OGLL-NGOA and parameters of KMGS (except the number of clusters and the weighting parameter) are illustrated in Table I.

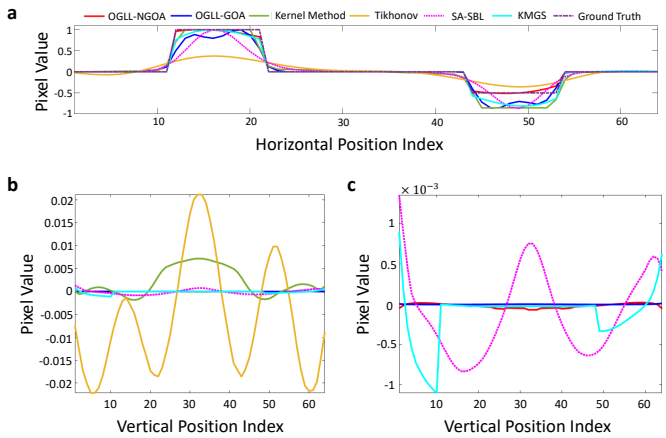

Fig. 6. 1D profile comparison for case 1. (a) shows 1D profiles on the horizontal line across the center of the imaging region. Both (b) and (c) display the 1D profiles on the vertical line across the imaging region center. All images share the same legend. The curve of OGLL-NGOA is invisible in (b) because it is hidden by other curves.

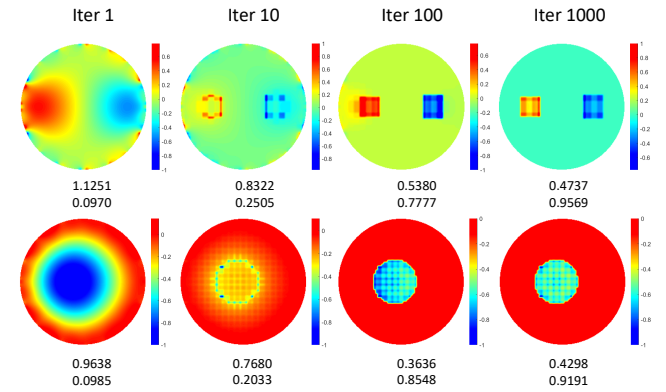

Fig. 7. GOA phenomenon in OGLL-GOA for case 1 and case 2 at selected iteration steps (1, 10, 100, 1000). For numbers under each image, the top one is Err and the bottom one is MSSIM.

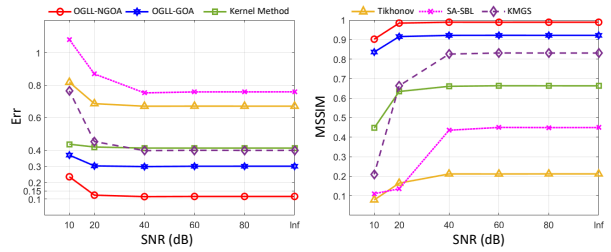

Fig. 8. Voltage noise resistance ability comparison: Err and MSSIM change with different SNRs. The plots share the same legends.

3) Results and Discussion: Fig. 3 compares OGLL with selected algorithms on the three cases. The voltage data is noise-free. The clustering results of the KMGS are shown in the second row of Fig. 4. Part of grouping results of OGLL is illustrated in Fig. 5. The results show the performance of single-modal based algorithms is generally inferior to the multi-modal based algorithms. This situation is indicated by visualization and quantitative metrics, i.e. the Err and MSSIM. The reason is that multi-modal methods utilize complementary information from other imaging modalities, mitigating the ill-

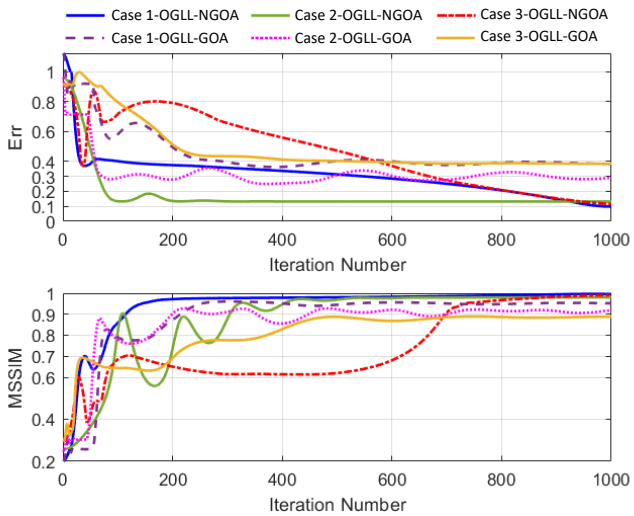

Fig. 9. Convergence curves: Err and MSSIM change with iterations.

posedness of the EIT inversion. Fig. 6 compares 1D profiles of case 1 of different algorithms. The results further visually demonstrate dual-modal methods are generally superior to single-modal methods. Among dual-modal methods, OGLL-NGOA achieves the best performance. OGLL-GOA also show a better BA suppression and competitive structure preservation ability compared to other algorithms. The quality of the reconstructed inclusions based on OGLL-GOA is similar to those based on Kernel Method and KMGS, while OGLL-GOA performs better than Kernel Method and is akin to KMGS on BA suppression. Nevertheless, quantitative metrics indicate the performance of both OGLL-GOA and OGLL-NGOA is generally superior than other given algorithms.

We demonstrate the effect of Laplacian regularization based on cases 1 and 2. Usually, the EIT image can be reconstructed well based on OGLL-NGOA. The reconstructed images of cases 1 and 2 based on OGLL-NGOA are shown in the seventh column of the Fig. 3. However, when we set $\theta = 0$ and keep other parameters for OGLL-GOA, GOA appears (see Fig. 7). The GOA originated from the search window size can hardly be eradicated by tuning other parameters and the results also show that such a phenomenon remains when iteration increases. Reconstructed images of OGLL-GOA with activated Laplacian regularization are displayed in the sixth column of the Fig. 3. These results indicate that Laplacian regularization mitigates the issue of GOA while the image quality degrades.The degradation of image quality is reasonable because the Laplacian regularization not only 'punishes' the GOA but also blurs edges of the inclusions. Nevertheless, it is conspicuous that OGLL provides flexible and controllable grouping and reconstruction strategies, and the Laplace regularization guarantees an accepted reconstruction when encountering the GOA.

Based on case 3, Fig. 8 compares the voltage noise resistance ability of algorithms. We set a serials of different SNRs for voltage data and display the Err and the MSSIM of given algorithms. The results demonstrate OGLL can resist the widest range of SNRs meanwhile maintaining best metric

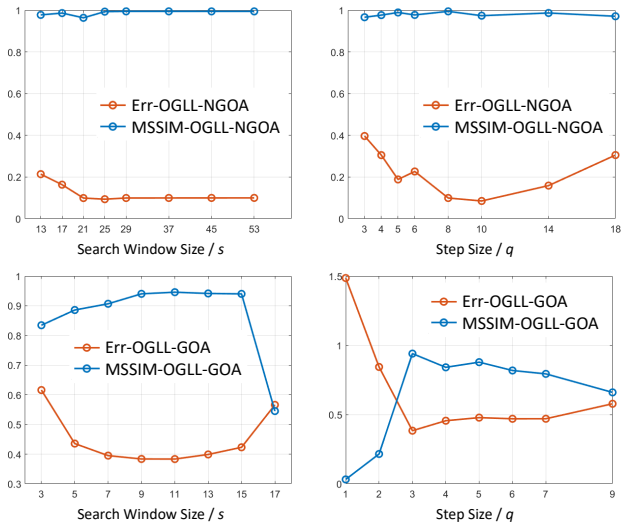

Fig. 10. Err and MSSIM variation with s and q change for OGLL-NGOA and OGLL-GOA.

values, which indicates the proposed OGLL has the best performance on voltage noise resistance.

The convergence analysis of OGLL are illustrated in Fig. 9. We observe that Err decreases with iterations and MSSIM increases with iterations, indicating the correct convergence property of the OGLL. However, oscillations exist due to two reasons. First, ADMM-based algorithms are not guaranteed monotonically decreasing [49]. Second, we use one-step gradient descent with fixed step length to solve the $\boldsymbol{\sigma}$-subproblem, which increases the possibility of having oscillation. Convergence curves vary with different cases since they are related to true conductivity distributions.

Fig. 10 takes case 1 as an example to analyse the influence of q and s on OGLL-NGOA and OGLL-GOA. Suppose suitable $\mathbf{f}_n$, ι and φ are defined, among OGLL parameters, s and q determine the grouping result, and further influence the reconstruction quality. Fig. 10 displays the Err and MSSIM variation with q or s meanwhile freezing other parameters. The results show there is a relatively wide range to select q or s while retaining a satisfactory result, indicating reduced complexity of parameter tuning.

There are several parameters to be tuned in OGLL. Therefore, it is worth introducing the parameter tuning experience. In this work, we adopt fixed η_1, η_2, $t_{\max}$, ϑ and φ, and always set the same values for β_1 and β_2. Only s, q, θ, α, and β_1 (or β_2) require tuning. The initial value of s is set according to the inclusion's size in the auxiliary image and q is set to $(s-1)/2$ to make groups partially overlap. In this study, the algorithm works correctly when we set the initial β_1 and β_2 both to 5. For both OGLL-NGOA and OGLL-GOA, the initial θ is set to 0. The next step is to select a reasonable starting point of α. One can begin from a large value, e.g. 100, and gradually decrease α by a factor of 0.1 until the quality of the reconstructed image improves with the increase of iterations. 0.01 is always selected as the initial α in this study. Afterwards, each parameter should be carefully tuned by the method of control variables.

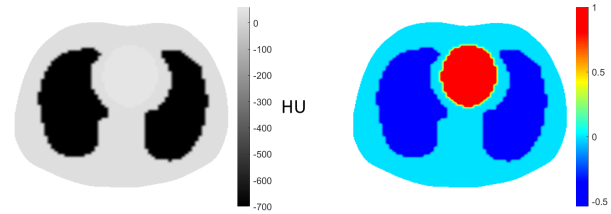

Fig. 11. The left image is the simulated CT image of the thoracic cross section and the right image is the simulated true thoracic EIT image.

TABLE II
PARAMETER SETTINGS OF OGLL AND KMGS FOR THORACIC IMAGING

	s	q	θ	α	β_1	β_2
KMGS	\	\	0	0.024	0.12	0.12
OGLL-NGOA	81	5	0	0.009	0.6	0.6
OGLL-GOA	31	5	0.15	0.007	0.25	0.25

C. Thoracic Imaging

1) Modelling: We modelled a cross-section of the human thorax to evaluate the performance of OGLL (see Fig. 11). Refer to [36], the surface contact impedance between electrodes and human skin is $10^{-4}\ \Omega \cdot m^{-1}$, and the left image of the Fig. 11 is the modeled CT image with 100 doses. Refer to [7], the background conductivity, the conductivity of lungs and the heart are set to 0.24 S/m, 0.1 S/m and 0.5 S/m, respectively. The ground truth image is the right image of Fig. 11.

2) Parameter Settings: Parameter settings are based on trial and error. For Tihkonov regularization, the regularization parameter is set to 0.0005. For SA-SBL, the maximum iteration number, tolerance, the cluster size, and the pattern coupling factor are set as 5, 10^{-5}, 4 and 0.16, respectively. For Kernel Method, the search window size and variance of the Gaussian kernel are set as 37 and 10, respectively. Other parameters are the same as those in the blocky phantom study. The weighting parameter for modified K-Means clustering in KMGS is 0.001

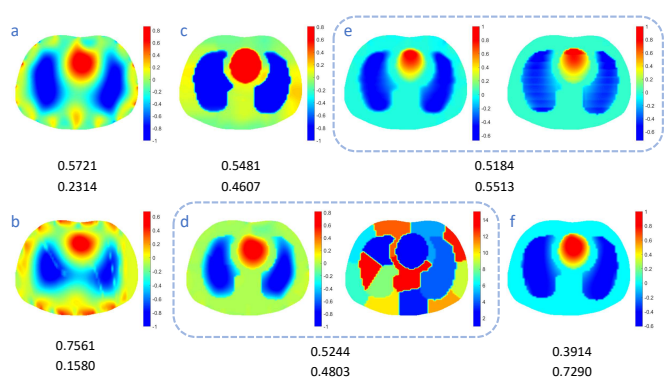

Fig. 12. Comparison of thoracic EIT image reconstruction. (a) ∼ (f) sequentially correspond to results of Tikhonov regularization, SA-SBL, Kernel Method, KMGS, OGLL-GOA and OGLL-NGOA. For (d) the left image is the reconstruction and the right is the result of K-Means clustering. There are 15 clusters. For (e), the left image is the reconstruction with Laplacian regularization and the right one is the reconstructed image without Laplacian regularization. For numbers under the result of each algorithm, the upper one is Err and the lower one is MSSIM. There are 138 groups for both OGLL-NGOA and OGLL-GOA.

TABLE III
PARAMETER SETTINGS OF OGLL AND KMGS FOR EXPERIMENTAL PHANTOM IMAGING

		s	q	θ	α	β_1	β_2
KMGS	Case 1	\	\	0	0.035	0.08	0.08
	Case 2	\	\	0	0.035	0.05	0.05
	Case 3	\	\	0	0.04	0.045	0.045
OGLL-NGOA	Case 1	29	8	0	0.008	0.1	0.1
	Case 2	29	8	0	0.008	0.17	0.17
	Case 3	29	8	0	0.008	0.08	0.08
OGLL-GOA	Case 1	11	4	0.3	0.01	0.25	0.25
	Case 2	15	4	0.1	0.008	0.3	0.3
	Case 3	17	5	0.04	0.008	0.25	0.25

and the number of clusters is 15. Other parameters of KMGS and parameters of OGLL-NGOA and OGLL-GOA are given in Table II. Parameters not shown in Table II are the same as those in Table I.

3) Results and Discussion: The reconstructed EIT images and quantitative metrics are shown in Fig. 12. The result of SA-SBL is poor. There are two main reasons. First, BA is severe for the irregular sensing region. Second, SA-SBL is more suitable for sparse conductivity distribution rather than non-sparse situations. The Kernel method reconstructs the most homogeneous lungs and heart among given algorithms while non-sparse background is noticeable. These phenomena are also clearly indicated in Fig. 6. For Fig. 12 (e), GOA is alleviated by the Laplacian regularization, which is consistent with the blocky phantom study. Compared with other algorithms, OGLL-NGOA and OGLL-GOA present superior performance, evidenced by quantitative metrics. Especially, OGLL-NGOA and OGLL-GOA recover the most accurate conductivity contrast levels, by comparing the color distribution of the reconstructed image with the ground truth.

V. REAL-WORLD EXPERIMENTS

A. Phantom Fabrication and Data Collection

In experiments, we used phosphate buffered saline as the reference conductivity (1.898 S/m). A total of five objects were selected and added to the imaging region into three groups labelled as case 1, case 2 and case 3 from top to bottom in the first column of Fig. 13. The first object is a conductive hexagonal prism (red arrow in figure), whose conductivity is higher than the saline. The other objects are either non-conductive regular prisms/cylinders or non-conductive irregular prisms/cylinders, whose conductivities are lower than saline. Non-conductive objects were fabricated using stereolithography (SLA) with black resin (FormLabs Inc., MA).

EIT data were collected using the Edinburgh EIT system [50]. The adjacent strategy was adopted [51] and the frequency of the excitation current was 10 kHz. A digital camera placed over the EIT sensor was used to collect the auxiliary images. The direct outputs of the camera are RGB images. We first converted them into gray-scale images (we call them original auxiliary images). We down-sampled the original auxiliary images into the EIT image size to acquire the expected auxiliary images. The original auxiliary images are illustrated in the first row of Fig. 14.

B. Parameter Settings

Parameter selection for each algorithm is based on trial and error. For all experiments, the Tihkonov regularization parameter is set to 0.005. For SA-SBL, the maximum iteration number, tolerance, the cluster size, and the pattern coupling factor are set as 5, 10^{-5}, 4 and 0.03 for all cases. Regarding the Kernel Method, variances of the Gaussian kernel are set to 18, 3 and 3 for case 1, case 2 and case 3 respectively. Other parameters are the same as those described in 2)-B, Section IV. The number of clusters for modified K-Means in KMGS is 30 for all cases and the values of the weighting parameter are 0.08, 0.08 and 0.065 for case 1, 2, and 3, respectively. Parameters of OGLL and KMGS related to ADMM are given in Table III. Parameters not shown in Table III are the same as those in Table I.

C. Results and Discussion

Fig. 13 shows the EIT image reconstruction results. The clustering results of KMGS are given in the second row of Fig. 14. In Fig. 13, there are two columns for OGLL-GOA. The left column is the reconstructed images with the Laplacian regularization and the right column is the reconstructed images without the Laplacian regularization. Compared with dual-modal methods, single-modal algorithms have less ability on structure preservation. Similarly to the simulation, the kernel method can reconstruct phantoms with homogeneous conductivity distribution but has limitations in eliminating the BA. The KMGS performs better than the kernel method while it is inferior to OGLL-NGOA, which can be indicated by the homogeneity of the background and objects. For OGLL-GOA, when we set the θ to non-zero numbers, the GOA is reduced. These experimental results further prove the effectiveness of the Laplacian regularization to mitigate the GOA though losing part of structural information. Nevertheless, OGLL-GOA generates EIT images close to the ground truth.

It is noticeable the boundaries in the auxiliary images are distinct in simulation and real experiments in this study. Good structural image quality could usually be gained for common auxiliary imaging modalities, such as CT and optical imaging. Therefore, $\mathbf{f}_n$ and ι adopted in this work can perform well in these situations. However, when the boundaries in the auxiliary images are not clear, $\mathbf{f}_n$ and ι used in this work may lead to inaccurate grouping. Therefore, new definitions of $\mathbf{f}_n$ and ι should be investigated.

VI. CONCLUSION

This paper proposes a segmentation-free dual-modal EIT image reconstruction algorithm named OGLL. OGLL integrates the structural information of the auxiliary image into EIT inversion through overlapping group lasso. Combining the overlapping group lasso with Laplacian regularization, the choice range of the grouping parameters is expanded. Simulation studies and real-world experiments demonstrate the superiority of the proposed OGLL on improving the EIT image quality in terms of structure preservation, background artifact suppression, and conductivity contrast differentiation. Future work will extend this method to 3D image reconstruction and

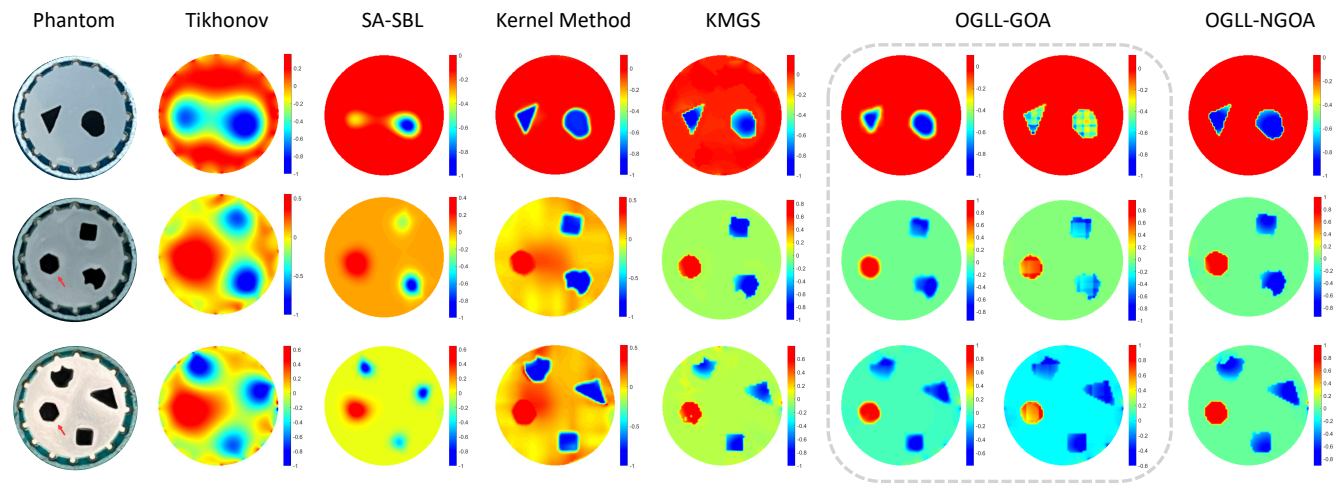

Fig. 13. Image reconstruction results based on experimental data. Results from top to bottom corresponds to case 1, case 2 and case 3 sequentially. Conductive hexagonal prism is indicated by red arrow. For both case 1 and case 2, the number of groups is 47 for OGLL-NGOA and is 201 for OGLL-GOA; and for case 3, the number of groups is 47 for OGLL-NGOA and is 129 for OGLL-GOA.

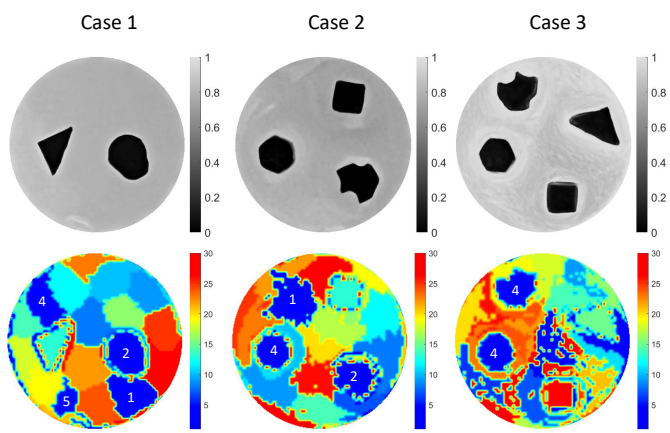

Fig. 14. Images in the upper row are original auxiliary images and those in the lower row are results of modified K-Means of KMGS.

explore its application in 3D cell culture imaging. In addition, $\mathbf{f}_n$ and ι definitions for various auxiliary imaging modalities will also be comprehensively investigated in the future.

Appendix

In EIT, the voltage changes $\Delta\mathbf{V} \in \mathbb{R}^M$ on the boundary electrodes are related to the conductivity changes $\Delta\boldsymbol{\sigma} \in \mathbb{R}^N$ from a reference homogeneous conductivity distribution by the following expression:

$$\Delta\mathbf{V} = \boldsymbol{\mathcal{J}}\Delta\boldsymbol{\sigma}, \tag{26}$$

where $\Delta\mathbf{V} = \mathbf{V}_o - \mathbf{V}_r$ and $\Delta\boldsymbol{\sigma} = \boldsymbol{\sigma}_o - \boldsymbol{\sigma}_r$. $\boldsymbol{\mathcal{J}} \in \mathbb{R}^{M\times N}$ stands for the ordinary sensitivity matrix, which is readily expressed as [52]:

$$\boldsymbol{\mathcal{J}}(j^{\tau\varrho},\ v) = -\int_{\mho_v} \nabla u^{\tau}(p)\cdot\nabla u^{\varrho}(p)d\omega, \tag{27}$$

where $u^{\tau}(p)$ and $u^{\varrho}(p)$ represent the electrical potential distribution in $\mho$ when the current is injected into the electrode pair $(e_{\tau},\ e_{\tau+1})$ and $(e_{\varrho},\ e_{\varrho+1})$, respectively. τ or $\varrho = 1,\ 2,\ \ldots, E$, and we define $e_{E+1} := e_1$. $j^{\tau\varrho}$ represents $(j^{\tau\varrho})^{\text{th}}$ measurement and $\mho_v$ denotes the region of the vth simplex.

Consider an assistant time point when the conductivity distribution $\boldsymbol{\sigma}_a$ is homogeneous and the corresponding voltage data is $\mathbf{V}_a$. Below equation also holds:

$$\mathbf{V}_a - \mathbf{V}_r = \boldsymbol{\mathcal{J}}\left(\boldsymbol{\sigma}_a - \boldsymbol{\sigma}_r\right). \tag{28}$$

As $\boldsymbol{\sigma}_a$ and $\boldsymbol{\sigma}_r$ are homogeneous, $\boldsymbol{\sigma}_a$ and $\boldsymbol{\sigma}_r$ can be rewritten as:

$$\begin{cases}\boldsymbol{\sigma}_a = \mathbf{1}_N\sigma_a\\ \boldsymbol{\sigma}_r = \mathbf{1}_N\sigma_r,\end{cases} \tag{29}$$

where $\mathbf{1}_N$ denotes the column 1-vector with N elements. $\sigma_a \in \mathbb{R}$ and $\sigma_r \in \mathbb{R}$ represent the conductivity values at the assistant and reference time points, respectively.

Combining (26) $\sim$ (29), lead to the following relationship:

$$\begin{aligned}\frac{\mathbf{V}_o - \mathbf{V}_r}{\mathbf{V}_a - \mathbf{V}_r} &= \frac{\boldsymbol{\mathcal{J}}\left(\boldsymbol{\sigma}_o - \boldsymbol{\sigma}_r\right)}{\boldsymbol{\mathcal{J}}\left(\boldsymbol{\sigma}_a - \boldsymbol{\sigma}_r\right)}\\ &= \frac{\boldsymbol{\mathcal{J}}\left(\boldsymbol{\sigma}_o - \boldsymbol{\sigma}_r\right)}{\boldsymbol{\mathcal{J}}\mathbf{1}_N\left(\sigma_a - \sigma_r\right)}\\ &= \left[\boldsymbol{\mathcal{J}}./\left(\boldsymbol{\mathcal{J}}\mathbf{1}_N\right)\right]\frac{\boldsymbol{\sigma}_o - \boldsymbol{\sigma}_r}{\sigma_a - \sigma_r},\end{aligned} \tag{30}$$

where './' means each element in a row of $\boldsymbol{\mathcal{J}}$, e.g. the mth row, is divided by the mth element of $\boldsymbol{\mathcal{J}}\mathbf{1}_N$. We denote $\boldsymbol{\mathcal{J}}./\left(\boldsymbol{\mathcal{J}}\mathbf{1}_N\right)$ as $\mathbf{J}$, and (30) becomes:

$$\frac{\mathbf{V}_o - \mathbf{V}_r}{\mathbf{V}_a - \mathbf{V}_r} = \mathbf{J}\frac{\boldsymbol{\sigma}_o - \boldsymbol{\sigma}_r}{\sigma_a - \sigma_r}. \tag{31}$$

Suppose $\sigma_a = \zeta\sigma_r$, then $\mathbf{V}_a = \frac{1}{\zeta}\mathbf{V}_r$, where $\zeta \in \mathbb{R}^+$. Therefore, (31) is converted into:

$$\frac{\mathbf{V}_o - \mathbf{V}_r}{\mathbf{V}_r} = \frac{1-\zeta}{\zeta^2 - \zeta}\mathbf{J}\frac{\boldsymbol{\sigma}_o - \boldsymbol{\sigma}_r}{\sigma_r}. \tag{32}$$

When $\zeta \to 1$:

$$\begin{aligned}\frac{\mathbf{V}_o - \mathbf{V}_r}{\mathbf{V}_r} &= \left(\lim_{\zeta\to 1}\frac{1-\zeta}{\zeta^2-\zeta}\right)\mathbf{J}\frac{\boldsymbol{\sigma}_o - \boldsymbol{\sigma}_r}{\sigma_r} \\ &= -\mathbf{J}\frac{\boldsymbol{\sigma}_o - \boldsymbol{\sigma}_r}{\sigma_r} \\ &= -\mathbf{J}\frac{\boldsymbol{\sigma}_o - \boldsymbol{\sigma}_r}{\boldsymbol{\sigma}_r}.\end{aligned} \tag{33}$$

It is readily acquiring the equation:

$$-\frac{\mathbf{V}_o - \mathbf{V}_r}{\mathbf{V}_r} = \mathbf{J}\frac{\boldsymbol{\sigma}_o - \boldsymbol{\sigma}_r}{\boldsymbol{\sigma}_r}. \tag{34}$$

Therefore, (6) holds.

References

[1] M. Cheney *et al.*, "Electrical impedance tomography," *SIAM review*, vol. 41, no. 1, pp. 85-101, 1999.

[2] R. H. Bayford, "Bioimpedance tomography (electrical impedance tomography)," *Annu. Rev. Biomed. Eng.*, vol. 8, pp. 63-91, 2006.

[3] P. Metherall *et al.*, "Three-dimensional electrical impedance tomography," *Nature*, vol. 380, no. 6574, pp. 509-512, 1996.

[4] G. Muehllehner, and J. S. Karp, "Positron emission tomography," *Physics in Medicine & Biology*, vol. 51, no. 13, pp. R117, 2006.

[5] A. F. Fercher, "Optical coherence tomography," *Journal of Biomedical Optics*, vol. 1, no. 2, pp. 157-173, 1996.

[6] I. Frerichs *et al.*, "Regional lung perfusion as determined by electrical impedance tomography in comparison with electron beam CT imaging," *IEEE transactions on medical imaging*, vol. 21, no. 6, pp. 646-652, 2002.

[7] K. Zhang *et al.*, "Supervised descent learning for thoracic electrical impedance tomography," *IEEE Transactions on Biomedical Engineering*, vol. 68, no. 4, pp. 1360-1369, 2020.

[8] E. Ravagli *et al.*, "Imaging fascicular organization of rat sciatic nerves with fast neural electrical impedance tomography," *Nature communications*, vol. 11, no. 1, pp. 1-10, 2020.

[9] K. Aristovich *et al.*, "Imaging fast neural traffic at fascicular level with electrical impedance tomography: proof of principle in rat sciatic nerve," *Journal of neural engineering*, vol. 15, no. 5, pp. 056025, 2018.

[10] Y. Yang *et al.*, "A miniature electrical impedance tomography sensor and 3-D image reconstruction for cell imaging," *IEEE Sensors Journal*, vol. 17, no. 2, pp. 514-523, 2016.

[11] Y. Yang *et al.*, "Scaffold-based 3-d cell culture imaging using a miniature electrical impedance tomography sensor," *IEEE Sensors Journal*, vol. 19, no. 20, pp. 9071-9080, 2019.

[12] H. Wu *et al.*, "Electrical impedance tomography for real-time and label-free cellular viability assays of 3D tumour spheroids," *Analyst*, vol. 143, no. 17, pp. 4189-4198, 2018.

[13] M. Wang *et al.*, "A high-performance EIT system," *IEEE Sensors Journal*, vol. 5, no. 2, pp. 289-299, 2005.

[14] H. McCann *et al.*, "A portable instrument for high-speed brain function imaging: FEITER," *2011 Annual International Conference of the IEEE Engineering in Medicine and Biology Society*, 2011, pp. 7029-7032, doi: 10.1109/IEMBS.2011.6091777.

[15] D. Chen *et al.*, "Design of impedance measuring circuits based on phase-sensitive demodulation technique," *IEEE Transactions on Instrumentation and Measurement*, vol. 60, no. 4, pp. 1276-1282, 2010.

[16] A. Borsic *et al.*, "In Vivo Impedance Imaging with Total Variation Regularization," *IEEE Transactions on Medical Imaging*, vol. 29, no. 1, pp. 44-54, Jan. 2010, doi: 10.1109/TMI.2009.2022540.

[17] B. Gong et al., "Higher order total variation regularization for EIT reconstruction," *Medical & Biological Engineering & Computing*, vol. 56, no. 8, pp. 1367-1378, 2018.

[18] G. González *et al.*, "Isotropic and anisotropic total variation regularization in electrical impedance tomography," *Computers & Mathematics with Applications*, vol. 74, no. 3, pp. 564-576, 2017.

[19] J. Li *et al.*, "Adaptive L_p regularization for electrical impedance tomography," *IEEE Sensors Journal*, vol. 19, no. 24, pp. 12297-12305, 2019.

[20] Q. Wang *et al.*, "Image reconstruction based on L1 regularization and projection methods for electrical impedance tomography," *Review of scientific instruments*, vol. 83, no. 10, pp. 104707, 2012.

[21] B. Jin *et al.*, "A reconstruction algorithm for electrical impedance tomography based on sparsity regularization," *International Journal for Numerical Methods in Engineering*, vol. 89, no. 3, pp. 337-353, 2012.

[22] K. Zhang *et al.*, "Three-dimensional electrical impedance tomography with multiplicative regularization," *IEEE Transactions on Biomedical Engineering*, vol. 66, no. 9, pp. 2470-2480, 2019.

[23] Y. Yang, and J. Jia, "An image reconstruction algorithm for electrical impedance tomography using adaptive group sparsity constraint," *IEEE Transactions on Instrumentation and Measurement*, vol. 66, no. 9, pp. 2295-2305, 2017.

[24] Y. Yang *et al.*, "Image reconstruction for electrical impedance tomography using enhanced adaptive group sparsity with total variation," *IEEE Sensors Journal*, vol. 17, no. 17, pp. 5589-5598, 2017.

[25] M. Alsaker *et al.*, "A direct D-bar method for partial boundary data electrical impedance tomography with a priori information," *Inverse Problems & Imaging*, vol. 11, no. 3, pp. 427, 2017.

[26] S. J. Hamilton *et al.*, "Incorporating a spatial prior into nonlinear D-bar EIT imaging for complex admittivities," *IEEE transactions on medical imaging*, vol. 36, no. 2, pp. 457-466, 2016.

[27] S. Liu *et al.*, "Image reconstruction in electrical impedance tomography based on structure-aware sparse Bayesian learning," *IEEE transactions on medical imaging*, vol. 37, no. 9, pp. 2090-2102, 2018.

[28] S. Liu *et al.*, "Accelerated structure-aware sparse Bayesian learning for three-dimensional electrical impedance tomography," *IEEE Transactions on Industrial Informatics*, vol. 15, no. 9, pp. 5033-5041, 2019.

[29] A. Adler *et al.*, "GREIT: a unified approach to 2D linear EIT reconstruction of lung images," *Physiological measurement*, vol. 30, no. 6, pp. S35, 2009.

[30] Z. Chen *et al.*, "MMV-Net: A Multiple Measurement Vector Network for Multifrequency Electrical Impedance Tomography," *IEEE Transactions on Neural Networks and Learning Systems*, doi: 10.1109/TNNLS.2022.3154108.

[31] F. Li *et al.*, "Electrical Resistance Tomography Image Reconstruction with Densely Connected Convolutional Neural Network," *IEEE Transactions on Instrumentation and Measurement*, vol. 70, pp. 1-11, 2021, Art no. 4500811, doi: 10.1109/TIM.2020.3013056.

[32] S. J. Hamilton, and A. Hauptmann, "Deep D-bar: Real-time electrical impedance tomography imaging with deep neural networks," *IEEE transactions on medical imaging*, vol. 37, no. 10, pp. 2367-2377, 2018.

[33] S. Ren *et al.*, "A statistical shape-constrained reconstruction framework for electrical impedance tomography," *IEEE transactions on medical imaging*, vol. 38, no. 10, pp. 2400-2410, 2019.

[34] G. Liang *et al.*, "An Inclusion Boundary and Conductivity Simultaneous Estimation Method for Ultrasound Reflection Guided Electrical Impedance Tomography," *IEEE Sensors Journal*, vol. 20, no. 19, pp. 11578-11587, 2020.

[35] S. Ren *et al.*, "A point constrained boundary reconstruction framework for ultrasound guided electrical impedance tomography," *IEEE Transactions on Computational Imaging*, vol. 6, pp. 1336-1350, 2020.

[36] Z. Li *et al.*, "CT image-guided electrical impedance tomography for medical imaging," *IEEE transactions on medical imaging*, vol. 39, no. 6, pp. 1822-1832, 2019.

[37] B. Gong *et al.*, "Sparse regularization for EIT reconstruction incorporating structural information derived from medical imaging," *Physiological Measurement*, vol. 37, no. 6, pp. 843, 2016.

[38] Z. Liu, and Y. Yang, "Image Reconstruction of Electrical Impedance Tomography Based on Optical Image-Guided Group Sparsity," *IEEE Sensors Journal*, vol. 21, no. 19, pp. 21893-21902, 2021.

[39] Z. Liu, and Y. Yang, "Multi-modal Image Reconstruction of Electrical Impedance Tomography Using Kernel Method," *IEEE Transactions on Instrumentation and Measurement*, 2021.

[40] Z. Liu, and Y. Yang, "Image Reconstruction of Electrical Impedance Tomography Based on Optical Image-Guided Group Sparsity," *IEEE Sensors Journal*, vol. 21, no. 19, pp. 21893-21902, 2021.

[41] E. Somersalo *et al.*, "Existence and uniqueness for electrode models for electric current computed tomography," *SIAM Journal on Applied Mathematics*, vol. 52, no. 4, pp. 1023-1040, 1992.

[42] E. Woo *et al.*, "Finite-element method in electrical impedance tomography," *Medical and Biological Engineering and Computing*, vol. 32, no. 5, pp. 530-536, 1994.

[43] B. Brandstatter, "Jacobian calculation for electrical impedance tomography based on the reciprocity principle," *IEEE transactions on magnetics*, vol. 39, no. 3, pp. 1309-1312, 2003.

[44] J. Huang, and T. Zhang, "The benefit of group sparsity," *The Annals of Statistics*, vol. 38, no. 4, pp. 1978-2004, 2010.

[45] S. Boyd *et al.*, "Distributed optimization and statistical learning via the alternating direction method of multipliers," *Foundations and Trends in Machine learning*, vol. 3, no. 1, pp. 1-122, 2011.

[46] Y. Yang *et al.*, "Effect of structured packing on EIT image reconstruction," *2014 IEEE International Conference on Imaging Systems and Techniques (IST) Proceedings*, 2014, pp. 53-58, doi: 10.1109/IST.2014.6958445.

[47] G. H. Golub *et al.*, "Tikhonov regularization and total least squares," *SIAM journal on matrix analysis and applications*, vol. 21, no. 1, pp. 185-194, 1999.

[48] Z. Wang *et al.*, "Image quality assessment: from error visibility to structural similarity," *IEEE transactions on image processing*, vol. 13, no. 4, pp. 600-612, 2004.

[49] G. Wang and J. Qi, "Edge-Preserving PET Image Reconstruction Using Trust Optimization Transfer," *IEEE Transactions on Medical Imaging*, vol. 34, no. 4, pp. 930-939, April 2015.

[50] Y. Yang and J. Jia, "A multi-frequency electrical impedance tomography system for real-time 2D and 3D imaging," *Rev. Sci. Instrum.*, vol. 88, no. 8, Aug. 2017, Art. no. 085110.

[51] B. H. Brown and A. D. Seagar, "The Sheffield Data Collection System," *Clinical Physics and Physiological Measurement*, vol. 8, no. 4A, p. 91, 1987.

[52] N. Polydorides and W. R. B. Lionheart, "A MATLAB toolkit for threedimensional electrical impedance tomography: A contribution to the electrical impedance and diffuse optical reconstruction software project," *Meas. Sci. Technol.*, vol. 13, no. 12, pp. 1871–1883, Dec. 2002.